Geophysical Journal International

Geophys. J. Int. (2017) **209,** 1462–1475
Advance Access publication 2017 March 10
GJI Geodynamics and tectonics

doi: 10.1093/gji/ggx102

Stress memory effect in viscoelastic stagnant lid convection

V. Patočka,[1] O. Čadek,[1] P.J. Tackley[2] and H. Čížková[1]

[1]*Department of Geophysics, Faculty of Mathematics and Physics, Charles University, Prague, Czech Republic. E-mail: patocka.vojtech@gmail.com*
[2]*Institute of Geophysics, Department of Earth Sciences, ETH Zurich, Switzerland*

Accepted 2017 March 9. Received 2017 March 7; in original form 2016 October 3

SUMMARY

Present thermochemical convection models of planetary evolution often assume a purely viscous or viscoplastic rheology. Ignoring elasticity in the cold, outer boundary layer is, however, questionable since elastic effects may play an important role there and affect surface topography as well as the stress distribution within the stiff cold lithosphere. Here we present a modelling study focused on the combined effects of Maxwell viscoelastic rheology and a free surface in the stagnant lid planetary convection. We implemented viscoelastic rheology in the StagYY code using a tracer-based stress advection scheme that suppresses subgrid oscillations. We apply this code to perform thermal convection models of the cooling planetary mantles and we demonstrate that while the global characteristics of the mantle flow do not change significantly when including viscoelasticity, the stress state of the cold lithosphere may be substantially different. Transient cooling of an initially thin upper thermal boundary layer results in a complex layered stress structure due to the memory effects of viscoelastic rheology. The stress state of the lid may thus contain a record of the planetary thermal evolution.

Key words: Numerical solutions; Elasticity and anelasticity; Dynamics of lithosphere and mantle; Lithospheric flexure; Rheology: crust and lithosphere.

1 INTRODUCTION

Mantle dynamics of terrestrial planets is traditionally modelled using viscous or viscoplastic rheology with viscosity strongly dependent on temperature and pressure. High viscosity contrasts typical for present day temperatures result in stagnant lid convection (Solomatov 1995), which can explain the tectonic style of most terrestrial planets. Surface topography and gravitational field are the primary constraints on the internal structure and dynamics of terrestrial planets and both are strongly affected by the properties of the lid. A commonly used assumption that this lid is purely viscous or viscoplastic is, however, questionable. There are multiple lines of evidence that planetary lithospheres show elastic behaviour on geological time scales. For example, the height and width of a forebulge associated with subduction and the response of a sedimentary basin to surface loading can be successfully explained by the deflection of a thin elastic plate (Turcotte & Schubert 2002). Numerous studies have thus addressed the effects of elasticity on the topography and geoid induced by internal dynamics of a planet.

Zhong (2002) calculated the topography and geoid of a 3-D spherical viscoelastic shell with static internal loading, where this loading was derived from the distribution of thermal buoyancy computed with a viscous flow solver. A different approach for combining the calculation of small deformations of an elastic or viscoelastic spherical shell with a viscous mantle convection code is presented by Golle *et al.* (2012), who used normal tractions from the mantle convection simulation at a given depth as the boundary condition for the deformation of a thin elastic shell. A more advanced approach involves the fully viscoelastic treatment of mantle convection within the whole domain including the stagnant lid. Such an approach allows the inclusion of lateral variations in the thickness of the lithosphere and accounts for the possible feedback between viscoelastic features in the lithosphere and sublithospheric internal dynamics.

Convection of a viscoelastic material on a planetary mantle scale was first addressed by Ivins *et al.* (1982). Later, Harder (1991) performed numerical experiments with a Maxwell medium with constant viscosity, the main focus being on stationary solutions of thermal convection in a box with free slip boundaries. More elaborate models that could include pressure and temperature induced lateral variations of viscosity, nonlinear stress-dependent rheologies and variable thickness of the lithosphere emerged about a decade later. Muhlhaus & Regenauer-Lieb (2005) found no significant deviations of statistical steady states in convection models with nonlinear rheology; only the transient phase was influenced by considering viscoelasticity. Beuchert & Podladchikov (2010) demonstrated how elasticity broadens the region of effective stress associated with a cold temperature anomaly prescribed within the lithosphere. They also studied statistical steady state convection. All of the above studies assumed a free-slip surface. Thielmann *et al.* (2015) addressed the effects of viscoelasticity and a free surface on stagnant lid convection with temperature dependent viscosity. Their target parameters were mean stress in the lithosphere and thickness of the stress boundary layer. While the significance of a free surface

was clearly demonstrated, the effect of viscoelasticity seemed to be negligible for planetary parameters, as the resulting dependencies of target parameters were rather flat for Deborah numbers up to 1. The above mentioned works focus on the effect of viscoelasticity on the horizontally averaged stress profile or on global characteristics of convection such as the bottom and top Nusselt numbers. Little attention is paid to the effect of stress memory, initial thermal conditions and topography.

The main focus of this study is to provide a detailed analysis of the effects of viscoelasticity on surface topography and stress evolution within the parameter range characteristic of planetary mantles. We will introduce a new viscoelastic flow solver based on the formulation by Moresi *et al.* (2002), implemented in StagYY (Tackley 2008). With this tool we will first employ a simple compositional model of a cylinder (representing plume head) rising below a stiff lithosphere to evaluate the response of a viscoelastic lid to convective loading. This part is an extension of the viscous model introduced by Crameri *et al.* (2012) and it demonstrates what are the combined effects of elasticity and a free surface on the developed surface topography. We will compare the free surface topography of the viscoelastic models to the topography calculated using the traditional instantaneous viscous flow (IVF) approach (e.g. Kiefer *et al.* 1996), in which dynamic topography is assumed to be proportional to the normal component of surface traction. After examining the effects of elasticity on lithospheric deformation in this basic model we will move to a more elaborate description of the cooling of a planetary mantle. We will construct a model of thermal convection in a planetary mantle with a free surface and evaluate the effects of viscoelastic rheology on lithospheric stresses. We will focus on temporal changes in the stress distribution during planetary cooling and we will demonstrate how the stress memory of the lithosphere affects the formation of stress distribution in planetary mantles.

2 GOVERNING EQUATIONS AND NUMERICAL METHODS

We employ two types of models. First, we perform models of purely composition driven convection with a simple density load (labelled as RC). A compositionally buoyant cylinder represents a rising plume head and we evaluate the effects of elasticity and surface boundary condition on the topography. In the second group of numerical experiments (labelled TC) we use viscoelastic thermal convection models and concentrate on the stress evolution within the lithosphere.

2.1 Governing equations

We assume an incompressible fluid with infinite Prandtl number with following equations describing conservation of mass and momentum:

$$\nabla \cdot \boldsymbol{v} = 0, \tag{1}$$

$$-\nabla p + \nabla \cdot \boldsymbol{\tau} + \rho \boldsymbol{g} = 0. \tag{2}$$

Here $\boldsymbol{v}$ is the velocity, ρ density, p pressure, $\boldsymbol{g}$ gravitational acceleration and $\boldsymbol{\tau}$ deviatoric stress. In case of the compositional models (RC) we further require the conservation of composition:

$$\frac{\partial c_k}{\partial t} + \boldsymbol{v} \cdot \nabla c_k = 0, \tag{3}$$

where c_k is the concentration (either 0 or 1) of kth material with the density ρ_k.

In the thermal convection models (TC), eqs (1) and (2) are supplemented by conservation of energy in the Boussinesq approximation:

$$\frac{\partial T}{\partial t} = \kappa \triangle T - \boldsymbol{v} \cdot \nabla T, \tag{4}$$

and a linearized equation of state:

$$\rho = \rho_0 (1 - \alpha (T - T_0)), \tag{5}$$

where T is the temperature, κ is the diffusivity, α is the thermal expansivity and ρ_0 is the density at reference temperature T_0. Both thermal expansivity and diffusivity are assumed constant.

2.2 Maxwell viscoelastic rheology

The rheological description of a Maxwell viscoelastic material is given by

$$\mathbb{D} = \mathbb{D}_{\text{viscous}} + \mathbb{D}_{\text{elastic}} = \frac{1}{2\eta(p_0, T)} \boldsymbol{\tau} + \frac{1}{2G} \frac{\mathcal{D}\boldsymbol{\tau}}{\mathcal{D}t}, \tag{6}$$

where $\mathbb{D}$ is the deviatoric part of the strain rate tensor, $\eta(p_0, T)$ is the viscosity dependent on temperature and hydrostatic pressure p_0, and G is the shear modulus. $\frac{\mathcal{D}}{\mathcal{D}t}$ denotes an objective tensor rate (e.g. Liu & Sampaio 2014). Here we adopt the Jaumann rate that is traditionally used in viscoelastic convection (see appendix A in Thielmann *et al.* 2015; Muhlhaus & Regenauer-Lieb 2005, for a discussion of objective rates in geodynamical context):

$$\frac{\mathcal{D}\boldsymbol{\tau}}{\mathcal{D}t} := \frac{\partial \boldsymbol{\tau}}{\partial t} + \boldsymbol{v} \cdot \nabla \boldsymbol{\tau} + (\boldsymbol{\tau}\mathbb{W} - \mathbb{W}\boldsymbol{\tau}), \tag{7}$$

where $\mathbb{W}$ is the antisymmetric part of the velocity gradient (spin tensor)

$$\mathbb{W} = \frac{1}{2} \left(\nabla \boldsymbol{v} - (\nabla \boldsymbol{v})^{\mathrm{T}} \right). \tag{8}$$

The corotational term $(\boldsymbol{\tau}\mathbb{W} - \mathbb{W}\boldsymbol{\tau})$ accounts for rotation of a volume element within the flow. Inserting (7) into (6) gives the following form of the constitutive equation:

$$2\eta\mathbb{D} = \boldsymbol{\tau} + \frac{\eta}{G} \left(\frac{\partial \boldsymbol{\tau}}{\partial t} + \boldsymbol{v} \cdot \nabla \boldsymbol{\tau} + \boldsymbol{\tau}\mathbb{W} - \mathbb{W}\boldsymbol{\tau} \right). \tag{9}$$

We consider an Arrhenius viscosity that depends exponentially on temperature and hydrostatic pressure p_0:

$$\eta(p_0, T) = \eta_0 \cdot \exp \left(\frac{E_{\text{act}} + p_0 V_{\text{act}}}{RT} \right), \tag{10}$$

where η_0 is set such that η is the reference viscosity at $T = 1600$ K and $p_0 = 0$ Pa, E_{act} is the activation energy, V_{act} is the activation volume and R is the gas constant. In viscous models that will be used as a reference to evaluate elasticity effects, $G \to \infty$ in eq. (9) and viscosity follows the same pressure and temperature dependency (eq. 10).

Following Moresi *et al.* (2002) we discretize eq. (9) with a mixed Euler first-order accurate scheme (implicit with respect to $\mathbb{D}$, $\boldsymbol{\tau}$ and viscosity, explicit with respect to advectional and corotational terms) and obtain the equation for stress in the nth time step:

$$\boldsymbol{\tau}^{\mathrm{n}} = 2Z\eta\mathbb{D}^{\mathrm{n}} + (1 - Z)\tilde{\boldsymbol{\tau}}^{\mathrm{n}-1}, \tag{11}$$

$$\tilde{\boldsymbol{\tau}}^{\mathrm{n}-1} := \boldsymbol{\tau}^{\mathrm{n}-1} - \triangle t \left(\boldsymbol{v} \cdot \nabla \boldsymbol{\tau} + \boldsymbol{\tau}\mathbb{W} - \mathbb{W}\boldsymbol{\tau} \right)^{\mathrm{n}-1}, \tag{12}$$

$$Z = \frac{\triangle t}{\triangle t + \eta/G}. \tag{13}$$

The implementation of viscoelasticity into a viscous flow code thus consists of replacing viscosity by numerical viscosity $\eta_{\rm num} := Z\eta$ and evaluating an extra term $\nabla \cdot [(1 - Z)\tilde{\boldsymbol{\tau}}^{\rm n-1}]$, which accounts for the effect of stress that did not fully relax within one time step. The importance of elastic effects is measured by viscoelasticity parameter Z that is closely related to the Maxwell relaxation time $t_{\rm M} = \eta/G$ ($Z \to 1$ when $\eta/G \ll \triangle t$). In non-dimensional studies, the role of $t_{\rm M}$ is played by the Deborah number, $De := \eta\kappa G^{-1} D^{-2}$, with D denoting the domain's depth.

Let us consider a constant value of the shear modulus, $G = 7 \times 10^{10}$ Pa (representative of the Earth's uppermost mantle). Then, for viscosity (in the mantle) equal to 10^{22} Pa s the relaxation time η/G is ∼4.5 kyr. With a typical computational time step of 100 kyr more than 95 per cent of stress is relaxed within one time step and the material behaves effectively as a viscous fluid. However, if the viscosity (in the lithosphere) is $\eta = 10^{27}$ Pa s, the relaxation time is ∼450 Myr and for the same computational time step only 0.02 per cent of stress is relaxed within one time step. Consequently, the material remembers its stress state from thousands of previous time steps.

In order to evaluate the differences between different viscous and viscoelastic models we introduce a scalar measure of stress, the second invariant of the stress tensor, which we will refer to as the effective stress:

$$\tau_{\rm eff} := \sqrt{\frac{\tau_{xx}^2 + \tau_{zz}^2}{2} + \tau_{xz}^2}, \tag{14}$$

with τ_{xx}, τ_{zz} and τ_{xz} denoting the Cartesian components of $\boldsymbol{\tau}$.

Time derivative of $\boldsymbol{\tau}$ in eq. (9) implies the need for an initial condition on the deviatoric stress. In all viscoelastic models we assume $\boldsymbol{\tau}(t = 0)$ equal to zero.

2.3 Numerical implementation

Numerical solution of the governing equations is performed using the code StagYY (Tackley 2008), which has been extended to include viscoelastic rheology by following the method described in Moresi *et al.* (2002) and Gerya & Yuen (2007). The method introduced by Moresi *et al.* (2002) and Moresi *et al.* (2003) was originally designed for finite elements. Here we apply it to a finite volume discretization (some aspects of stress evaluation accuracy in context of finite volume discretizations of elastic plate bending problems are discussed in Vaz *et al.* 2009). Benchmarks used to test the viscoelastic part of the code are presented in Appendix A. For technical details regarding the implementation we refer the reader to Gerya & Yuen (2007), deviations from their approach are described below.

We implemented both a grid-based and tracer-based advection of stress. Using particles for advecting a quantity is optimal when the quantity remains constant on each particle throughout the simulation. If so, only interpolation from tracers to grid is needed. This is not the case with the stress tensor in viscoelastic media: the first term on the right hand side of eq. (11) is a contribution that is computed each time step on the grid and is interpolated from grid to tracers. The convenience of tracer-based advection thus depends on the relative importance of the terms on the right hand side of eq. (11). It performs slightly better than the grid-based donor cell method when simulating the recovery of the original shape of an elastic slab (see Appendix A2), as the stresses only gradually build up in the slab and do not change much over computational time steps. The opposite is true when simulating the flow described in Appendix A1, especially for advecting stresses in regions of high vorticity on a sparse mesh. While the donor cell method leads to a satisfactory fit to the reference stationary flow described in Harder (1991), with tracer-based advection over a thousand tracers per cell are required to reach comparable solution quality. In the thermal convection simulations reported below we use tracers to advect stress tensor components, but we obtained qualitatively the same results with the donor cell advection scheme as well.

Our implementation of the tracer-based variant differs from Gerya & Yuen (2007) in the way the second term on the right hand side of eq. (11) is treated. In thermal convection simulations, subgrid oscillations of stress can occur in advection dominated regions. When the stress change is computed in a volume integrated sense (i.e. on the nodes of the mesh) and subsequently interpolated to tracers, then two tracers with a different stress history that at certain moment are very close to each other can unphysically retain a mutual stress jump even when entrained to an effectively viscous part of the domain (see Appendix B and Fig. B1 for more details). The problem is similar to the problem of subgrid oscillations of temperature when this quantity is carried on tracers but diffusion is computed on the mesh.

In order to reduce these oscillations Gerya & Yuen (2007) use subgrid diffusion, controlled by additional numerical parameters (see their eq. 24 and the preceding paragraph). Here we introduce a novel approach that performs the relaxation procedure, that is, multiplication by factor $(1 - Z)$ in eq. (11), directly on tracers and not on the grid. Only then is the second term in eq. (11) interpolated to the respective positions on the staggered grid. In effectively viscous regions this procedure leads to individually zeroing out the stress from the previous time step on each tracer, regardless of the value of stress on neighbouring tracers. As a result, the stress field is smooth and determined solely by $2Z\eta\mathbb{D}^{\rm n}$ in these regions. No additional (numerical) diffusion parameters are needed in our simulations.

Another important issue that determines numerical stability is the choice of time step. In the time-averaging approach of Moresi *et al.* (2003) the elastic time step $\triangle t$ in eqs (12) and (13) can in general be chosen independently on the advectional time step controlled by CFL condition. If one sets a lower bound on $\triangle t$ it means that material with relaxation time smaller than this limit value $\triangle t_{\rm min}$ behaves effectively as viscous medium (*cf.* eq. 11). This can help to stabilize the numerical simulations in certain cases (see section 'Elastic Timestep' in Moresi *et al.* (2002) for details). Here we however did not need to apply a lower bound $\triangle t_{\rm min}$ and use only one time step both in the constitutive equation and for advecting the tracers (see the discussion in Appendix A1). This time step is dictated by the CFL condition with Courant number equal to 0.5.

The tracers are advected using the fourth-order spatially accurate Runge–Kutta method. We use linear tracer to node interpolation for the diagonal components of the deviatoric stress (located at cell centres) and cell averaging interpolation for the off-diagonal components (located at grid vertices, resp. edge centres in 3-D).

To conclude this section, a note should be made of a positive side effect that comes with implementing viscoelasticity. The numerical viscosity, which numerically plays the role of physical viscosity when solving the Stokes equation, has much smaller spatial contrasts than the physical one (see Beuchert & Podladchikov 2010, for details). The pre-factor Z in eq. (13) is from the interval (0, 1), and decreases with increasing viscosity for a given time step. Thus $Z \doteq 0.95$ for mantle material with viscosity $\eta = 10^{22}$ Pa s and shear modulus $G = 7 \times 10^{10}$ Pa if the computational time step is 100 kyr, while $Z \doteq 0.0002$ for lithosphere with $\eta = 10^{27}$ Pa s and the same shear modulus, that is, reducing the viscosity

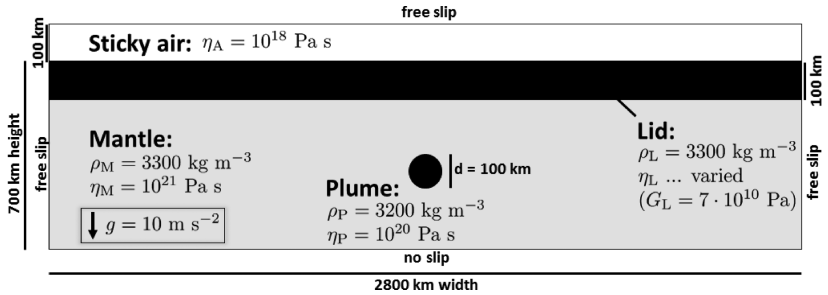

Figure 1. Model setup used in Section 3. Viscosity of the lid is varied. Simulations with viscoelastic rheology have constant shear modulus $G_L = 7 \times 10^{10}$ Pa. For free surface simulations sticky air layer of thickness 100 km and viscosity 10^{18} Pa s is employed.

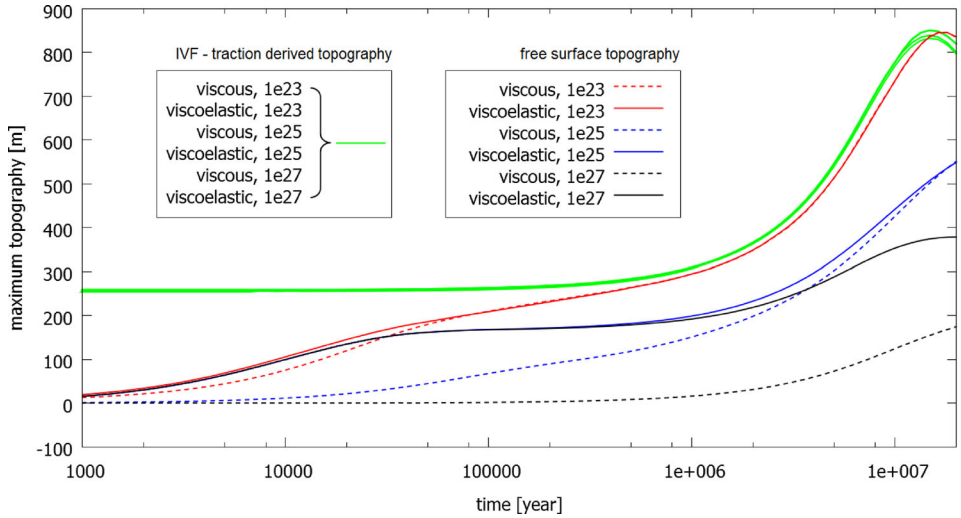

Figure 2. Topographic response to a rising cylinder, different colours stand for different values of η_L in Pa s. Solid lines show the evolution of maximum topography when viscoelastic rheology is employed, dashed lines are for viscous rheology. Red dashed curve is the response to Case 2 in Crameri *et al.* (2012). Green lines represent the overlapping, traction derived topographies.

contrast by four orders of magnitude. This improves the convergence of multigrid iterations when solving the resulting system of linear equations.

3 RISING CYLINDER (RC MODELS)

3.1 Model setup

We use the same model setup as Crameri *et al.* (2012), designed to mimic the interaction of the stiff lithosphere with a rising plume head. Our model domain is an isothermal 2-D box (2800 km × 700 km) with a no-slip bottom boundary and impermeable free-slip side boundaries (Fig. 1). Viscous mantle (600 km deep) with a viscosity of 10^{21} Pa s and density of 3300 kg m^{-3} is overlain by a 100 km thick, neutrally buoyant, viscoelastic lithosphere. We test three values of lithospheric viscosity: 10^{23}, 10^{25} and 10^{27} Pa s. The rising plume head is modelled as a less dense cylinder initially located in the middle of the mantle layer. The diameter of the cylinder is 100 km and it is characterized by a density of 3200 kg m^{-3} and a relatively low viscosity of 10^{20} Pa s. Viscoelastic models have shear modulus $G_L = 7 \times 10^{10}$ Pa in the viscoelastic lithosphere and their mantle is kept viscous (which is numerically achieved by using a high value of the shear modulus in the mantle, $G_M = 10^{20}$ Pa). We use a regular grid resolution with 256 × 1024 points and 100 particle tracers per cell.

Our models have either a free surface implemented using the sticky-air approach (Matsumoto & Tomoda 1983; Schmeling *et al.* 2008) or an impermeable free-slip surface. Sticky air is modelled as a 100 km thick layer of a very weak material ($\eta_A = 10^{18}$ Pa s) with negligible density ($\rho_A = 10^{-3}$ kg m^{-3}). Surface topography in the free surface models is calculated by tracking the interface between the lithosphere and sticky-air. In free-slip models the surface topography is assumed to be proportional to the normal component of surface traction (e.g. Kiefer *et al.* 1996)—we denote this here as the IVF response. For each lithospheric viscosity we run four models—with purely viscous or viscoelastic rheology and with a free surface or a free-slip surface. We use very fine time steps here, 20× smaller than the values dictated by the CFL stability condition, in order to resolve the initial evolution of topography.

3.2 Results: topography above a rising cylinder

First, let us discuss the topography developing above a cylinder rising through the mantle towards the stiff lithosphere (Fig. 1). We use this simple model to demonstrate the basic features of stress and topography development in a stiff layer loaded by a viscous upwelling. We vary the viscosity of the stiff lithosphere (10^{23}, 10^{25} and 10^{27} Pa s) and for each viscosity we perform both the IVF model (with impermeable free-slip surface) and the free surface model, and compare the resulting topographies.

The buoyant cylinder needs about 10 Myr to rise from its initial position towards the base of the lithosphere. During this time the traction acting at the bottom of the lid due to the load steadily increases. Fig. 2 depicts the maximum topography reached in the

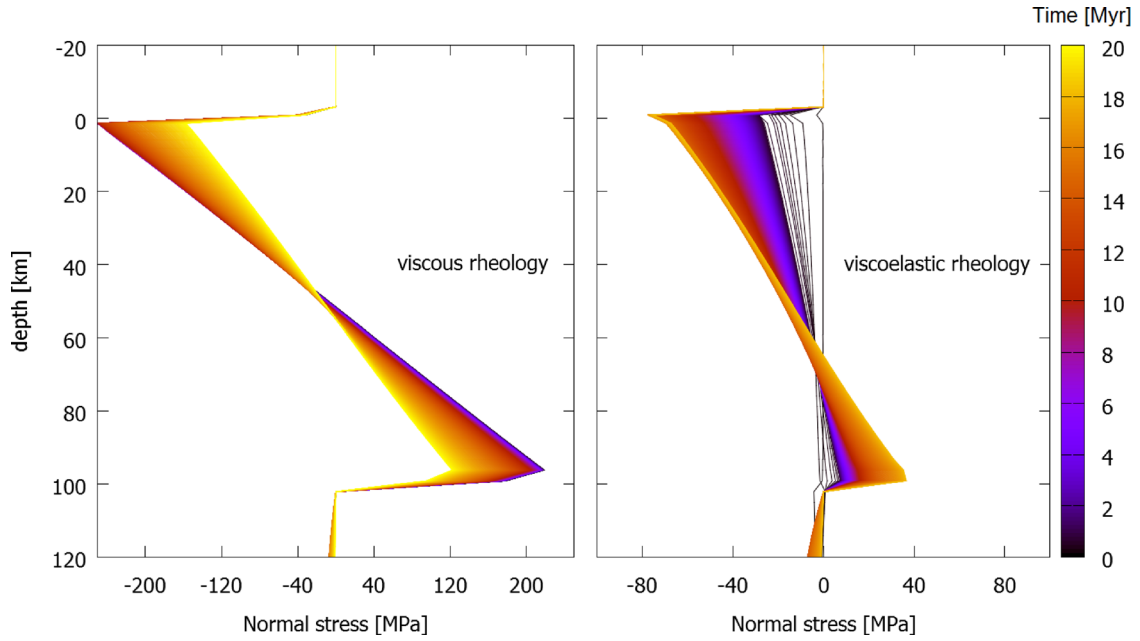

Figure 3. Temporal evolution of vertical deviatoric stress τ_{zz} in models with a free surface and η_L equal to 10^{27} Pa s. Left panel shows viscous model, right panel is for viscoelastic model. Stress is plotted as a function of depth along a vertical line located above the centre of the rising cylinder. Colour represents time in Myr.

middle of the box above the rising cylinder as a function of time. Solid lines show the viscoelastic models while dashed lines are for corresponding viscous models ($G_L \to \infty$). The IVF topographies are insensitive to lithospheric viscosity and almost identical for viscous and viscoelastic models. Viscoelastic material transfers stresses to the top free slip boundary in a similar way to viscous material when flexure is not allowed by the top boundary condition. The IVF topographies gradually increase as the load becomes closer to the surface and reach their maximum of about 800 m when the cylinder reaches the base of the lithosphere. Free-surface topographies (red, blue and black lines), on the other hand, do depend on the lithospheric viscosity and vary between the viscous and viscoelastic models. In case of the lowest lid viscosity (10^{23} Pa s, red line) the Maxwell relaxation time is ∼45 kyr and viscoelasticity thus plays little role. At the beginning both topographies quickly increase (time is displayed on logarithmic scale) and after few hundreds of kyr they get close to the IVF value, which they follow afterwards because the Stokes time scale is larger than the isostatic relaxation time of the lid (see Crameri *et al.* 2012, for details). Higher viscosity lids (10^{25} and 10^{27} Pa s; blue and black lines) already cause visible differences between viscous and viscoelastic models in topography development. Topographies in viscous models are significantly reduced with respect to the IVF response due to the resistance of a stiff lid to bending. Viscoelastic material on the other hand responds with elastic deformation as well and developed topography is higher (closer to IVF values). The large difference between the IVF and free-surface topography of purely viscous models demonstrates a drawback of the IVF approach: it yields topographies that are almost independent of the lid's viscosity, whereas free surface topographies differ significantly for lithospheric viscosities which are commonly used as cut-off values in geodynamical models.

The evolution of topography formed by the viscoelastic lids is determined by their respective Maxwell relaxation times (∼45 kyr for the solid red line, ∼4.5 Myr for the solid blue line, ∼450 Myr for the solid black line), with the exception of the initial rise, which is controlled by viscosity of the mantle. The viscous deformation of the mantle delays the (otherwise instantaneous) elastic flexure of the lid (cca 160 m for the initial position of the load). Weak lithosphere (solid red line) is characterized by a short Maxwell relaxation time, smaller than both the Stokes time scale of the rising cylinder and the isostatic relaxation time of a viscous lithosphere (for the given viscosity). The evolution of topography in viscoelastic cases with higher lithospheric viscosity (solid blue and solid black lines) is identical as long as the dominant deformation mechanism is the purely elastic one (i.e. mechanism insensitive to η_L). The lines separate as soon as viscoelastic relaxation starts to be significant for $\eta_L = 10^{25}$ Pa s, slowly increasing the observed topography by shifting from the elastic to the viscous limit. With $\eta_L = 10^{27}$ Pa s the Maxwell relaxation time is much larger than the duration of the simulation, and the solid black line thus represents a purely elastic response ($\eta_L \to \infty$). The effect of elastic filtering, described in Golle *et al.* (2012), addresses the difference between such response and a traction derived topography.

Fig. 3 demonstrates stress evolution within the lithosphere with a free surface. It shows the vertical deviatoric stress τ_{zz} as a function of depth plotted above the centre of the rising cylinder in a model with the strongest lithosphere ($\eta_L = 10^{27}$ Pa s). Colour represents time: black and dark colours are for the beginning of the calculation, while orange and yellow are for the time when the cylinder reaches the bottom of the lid. The left panel shows the viscous model, whereas the right panel is for the viscoelastic model. The initial stress in the viscous model is large (∼200 MPa) and the pattern corresponds to bending. The amplitude decreases as the cylinder rises and topography grows—the elevated surface of the lid counteracts the effect of the upward push of the cylinder.

In the viscoelastic lid the stresses are significantly smaller and they simply increase as the topography increases, because the stresses are fully determined by the total strain in the effectively elastic lid.

Table 1. Parameters used in the convection calculations.

Parameter	Symbol	Model E_{el}	Model M_{el}	Units
Mantle depth	D	2890	1666	km
Gravitational acceleration	g	9.81	3.7	m s^{-2}
Reference density	ρ_0	3300	3300	kg m^{-3}
Temperature drop	ΔT	2500	1500	K
Reference viscosity	η_{ref}	10^{23}	9.316×10^{19}	Pa s
Upper viscosity cut-off	η_{max}	10^{28}	10^{28}	Pa s
Thermal diffusivity	κ	7.6×10^{-7}	7.6×10^{-7}	m^2 s^{-1}
Thermal expansivity	α	3×10^{-5}	3×10^{-5}	K^{-1}
Activation energy	E_{act}	240	346	kJ mol^{-1}
Activation volume	V_{act}	8.9×10^{-7}	2×10^{-7}	m^3 mol
Surface temperature	T_{surf}	289	230	K
Shear modulus[a]	G	7×10^{10}	7×10^{10}	Pa

[a] Models E_{vis} and M_{vis} are obtained by setting $G \to \infty$.

4 THERMAL CONVECTION (TC MODELS)

4.1 Model setup

After examining the basic characteristics of a viscoelastic response in free-slip and free-surface models, we now proceed towards the convection models, in which the flow is driven by thermal buoyancy and the viscosity is controlled by the temperature distribution and the depth.

We concentrate on the effects of viscoelasticity on the transient behaviour of the stiff lid and demonstrate how viscoelasticity affects stress evolution in the lithosphere during its cooling and thickening. To that end we perform models of two planetary bodies with different reference viscosities and thus different vigour of convection in the transient phase. The first one is an Earth-sized body (E-models) with a relatively high η_{ref} and model parameters based on Crameri & Tackley (2014). The other one is a Mars-sized body (M-models) with lower η_{ref} and parameters taken from Golle *et al.* (2012). For each planet we test two scenarios – one with an initially thin lithosphere (controlled by the initial thermal boundary layer thickness $d_{TB} = 30$ km) and the other one with an initially 300 km thick lithosphere.

We assume basally heated convection with constant temperature top and bottom boundaries, while the sides are insulating with zero normal heat flux. The initial temperature distribution follows the relation:

$$T(z) = T_0 + (T_{surf} - T_0) \exp\left(\frac{-z}{d_{TB}}\right) + (T_{CMB} - T_0) \exp\left(\frac{z - D}{d_{TB}}\right), \quad (15)$$

where $T_0 = 1900$ K is the temperature at the mid-depth, T_{surf} and T_{CMB} are surface and core-mantle boundary temperatures, d_{TB} is the initial thickness of the thermal boundary layer, D is the mantle thickness and z is the depth. Random temperature perturbations with amplitude 20 K are used to initiate convection. The model parameters are summarized in Table 1.

Each convection simulation starts with a transient stage in which the sublithospheric flow evolves and the cold, stiff lithosphere gradually changes its thickness. Then, a statistically steady state is reached and the lithospheric thickness remains constant. The temperature T_0 in the mid-mantle is initially set to 1900 K. For E-models this is less than the statistically steady state mid-mantle temperature, thus the central part of the model heats up during transient phase and the vigour of convection increases. For the Mars-like parameter set, on the other hand, 1900 K represents an overheated mantle, mainly because of the smaller temperature drop between the core-mantle boundary and surface. Due to the lower reference viscosity, a vigorous, downwelling dominated convection initially develops in the model and is gradually quelled as the mid-mantle temperature decreases down to cca. 1700 K.

The model domain is a 2-D Cartesian box with aspect ratio 1 and a mantle depth of 2890 km for E-models and 1666 km for M-models. Impermeable free slip boundaries are assumed at the bottom and sides of the box. The top boundary is either assumed to be impermeable free slip, or similarly to the RC models, a free surface using the sticky-air approach. Following Crameri & Tackley (2014) we use a 150 km thick sticky-air layer with viscosity $\eta_A = 10^{21}$ Pa s (given our upper viscosity cut-off, this choice provides a reasonable balance between obtained accuracy and the length of computational time step necessary to avoid the 'drunken seaman' instability described by Kaus *et al.* 2010; Duretz *et al.* 2011). The mesh resolution is 256×256 nodes.

4.2 Results: free-slip surface

First let us discuss the Earth-size models with an impermeable free-slip surface and initially thin lithosphere. Fig. 4 shows a snapshot of viscosity in the whole model domain (left column), effective stress in the upper half of the model domain (middle column) and vertical deviatoric stress (right column), all taken after 4.6 Gyr. The upper row is for a purely viscous model E_{vis}, while bottom row is for a viscoelastic one E_{el}. Below the lithosphere the flow pattern is almost identical for both rheologies (see Fig. 5) and we can thus compare responses to almost identical loading. The viscous model results in a relatively simple smooth stress distribution within the stiff lithosphere that reflects the distribution of upwelling and downwelling features.

The viscoelastic model, on the other hand, shows a rather complex layered stress pattern in the lower part of the lithosphere in the middle between the two downwellings. The depth of the first 'layer' indicates the thickness to which the lithosphere cooled conductively with no accompanying deformation. The stress layers themselves formed during the thickening period and reflect the lateral movement of upwellings and downwellings during the history of the thickening lithosphere. In general, when viscoelastic lithosphere grows, the accretionary edge records the stresses caused by the upwelling and downwelling features active at the time of the accretion. These stresses are remembered, but they are also gradually altered as they relax and as new downwellings pull and new plumes push throughout the entire thickness of the lid. The thickness and lateral extent of the stress layers is determined by the spatial stability of the dynamical features relative to the characteristic time of the cooling.

In case of the Mars-like body more vigorous convection develops during the transition phase. The shorter wavelength structure of the downwellings in the sublithospheric mantle is also reflected in the stress pattern in the lithosphere, in both viscous and viscoelastic models. Fig. 6(a) shows the vertical stress component τ_{zz} at two snapshots taken during transient cooling and thickening of the lithosphere at 1 Gyr and at 2 Gyr. Clearly, a complex layered lithospheric stress pattern due to memory effects in a viscoelastic model (as described above) is much more pronounced here. This is due to the relative instability and characteristic wavelength of the downwellings. Additionally, the region of smooth stresses is significantly reduced when compared to the less vigorous Earth-sized model as the downwellings quickly develop in the early stages of the model

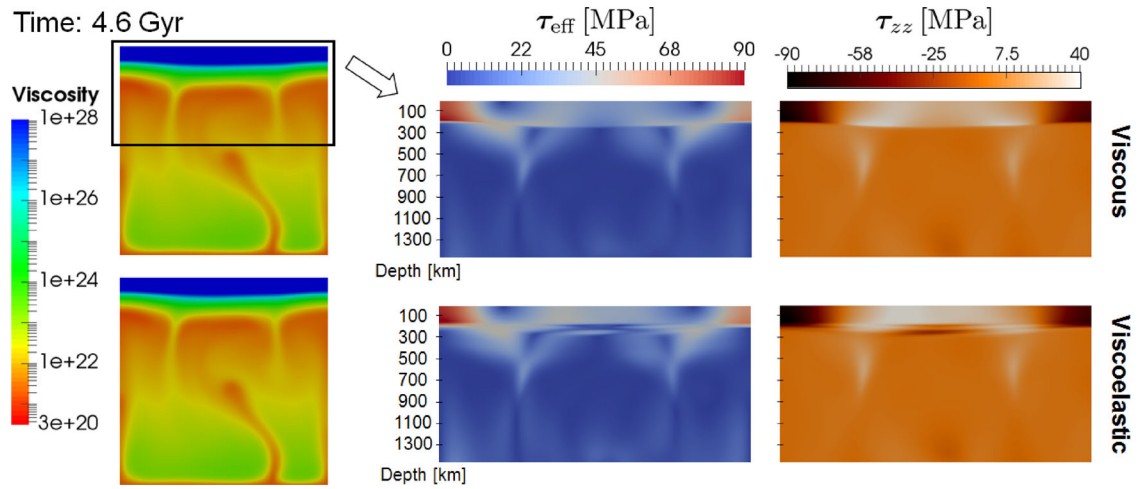

Figure 4. Model E with aspect ratio 1, $T_0 = 1900$ K, $d_{\rm TB} = 30$ km and a free slip upper boundary after approximately 4.6 Gyr. Top row shows the viscosity, effective stress and vertical deviatoric stress τ_{zz} of model $E_{\rm vis}$, bottom row shows the simulation with vicoelastic rheology ($E_{\rm el}$). Stresses are shown in upper part of the domain only, depth is in km.

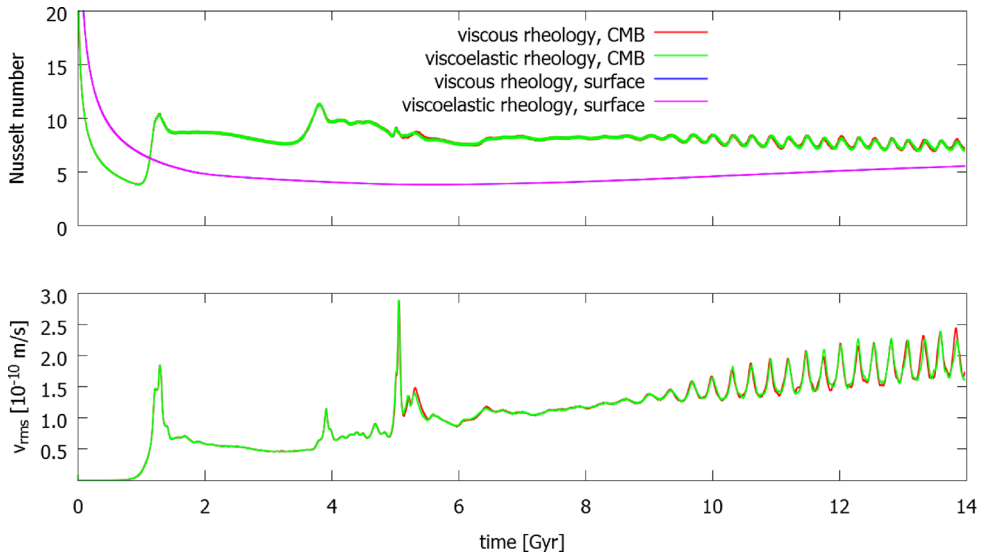

Figure 5. Top and bottom Nusselt numbers and mean velocities in models $E_{\rm vis}$ and $E_{\rm el}$ with aspect ratio 1, $T_0 = 1900$ K, $d_{\rm TB} = 30$ km and a free-slip upper boundary.

evolution. When a steady state is reached and lithospheric thickness does not increase further, frozen stress structures relax and within several Gyr this shallow, layered stress structure resulting from memory effects of viscoelastic rheology is no longer present. Viscoelastic models then have comparable stress magnitude and pattern as viscous ones. The time that the structure needs to disappear is related to the Maxwell relaxation time of the lithosphere (4.5 Gyr for the upper viscosity cut-off 10^{28} Pa s).

So far we have discussed the results of the models with an initially thin lithosphere. If we instead initially prescribe a thick lithosphere ($d_{\rm TB} = 300$ km) we observe none of the above described effects on stress development and the behaviour of viscoelastic models is the same as that of viscous models (see Fig. 6b).

4.3 Results: free surface

In the previous paragraph we described the results of the models with a free-slip surface. Now let us focus on the models with a free surface. Based on the results of our numerical experiments with a rising cylinder, we may expect much stronger effects of elasticity, as the lithospheric flexure can now fully develop.

Fig. 7 shows the stress evolution in the smaller Mars-like mantle models $M_{\rm vis}$ and $M_{\rm el}$ – with initially thin lithosphere $d_{\rm TB} = 30$ km. In a purely viscous model (left column) the stress pattern in the lithosphere reflects its bending due to the pull of the sublithospheric downwellings (no plumes are initially present due to the fact that the mantle is overheated). The wavelength of the lithospheric undulations is controlled by the temporary distribution of the downwellings and by the actual thickness of the lithosphere. As the lithosphere cools and thickens, the wavelength of the undulations generally increases. In a viscoelastic case (right column) the stress pattern is again much more complex. Stresses obtained during the bending of initially thin plate (easy to bend and thus reaching relatively large strains) are remembered ('frozen') until cca. 4 Gyr and during cooling and thickening of the lid its deeper parts adopt and remember the stresses due to later bending. The amplitude of the stress in the deeper layers is smaller than the amplitude of the initial surface stress layer due to the fact that the colder and thicker lid becomes

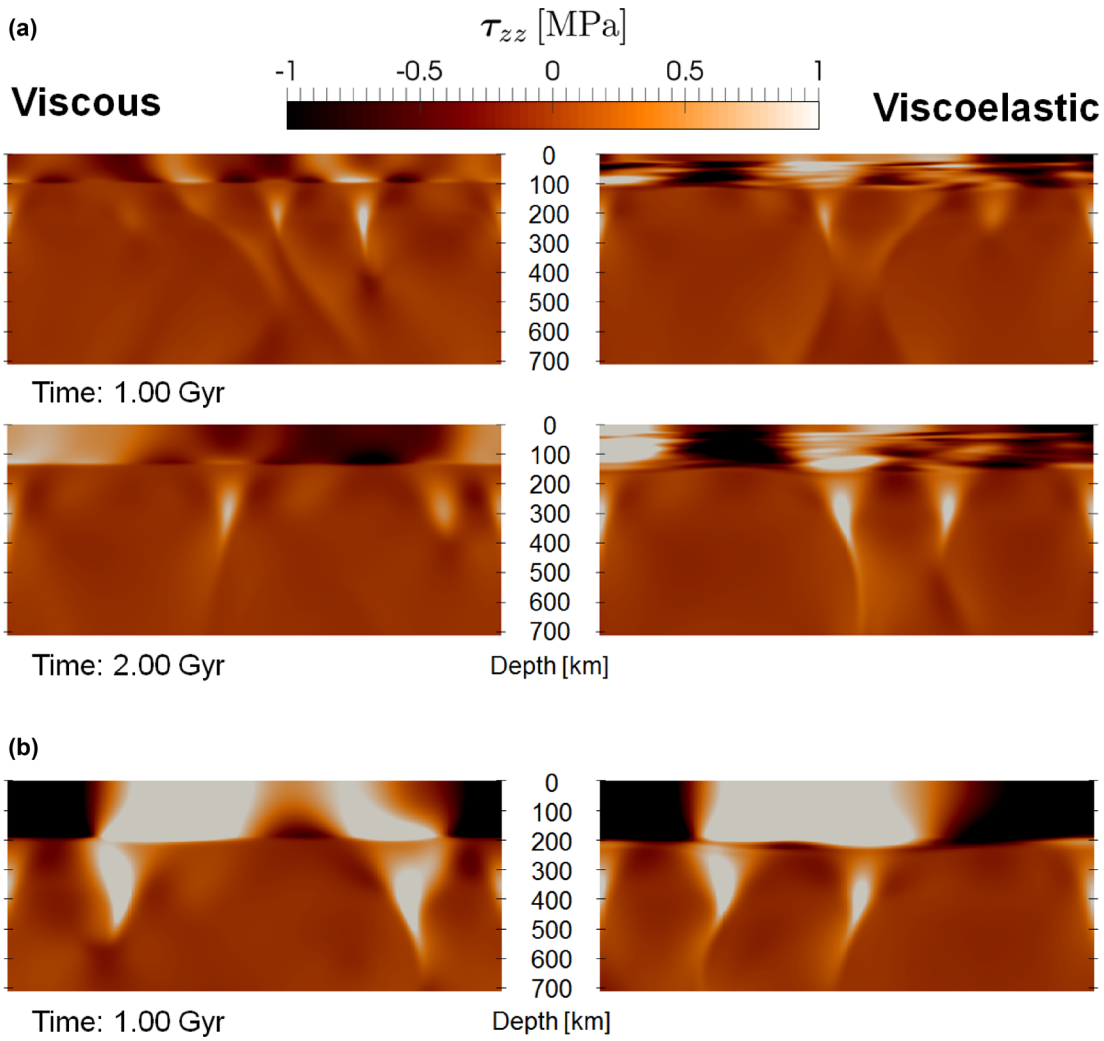

Figure 6. Normal stress component τ_{zz} in model $M_{\rm vis}$ (left column) and model $M_{\rm el}$ (right column) after cca. 1 Gyr (top row) and 2 Gyr (second row). Both models have aspect ratio 1, $T_0 = 1900$ K and a free-slip surface. Depths only down to 700 km are shown. Stress scale is clipped for better visibility of the memory effect. (a) Initially thin lithosphere is prescribed, with $d_{\rm TB} = 30$ km. (b) The case with initially thick lithosphere, $d_{\rm TB} = 300$ km.

increasingly difficult to bend. These large stresses are preserved on time scales comparable to the surface value of $t_{\rm M}$ (4.5 Gyr). After 3 Gyr mantle has cooled down enough and plumes start to develop. Large stresses associated with strong plumes pushing at the base of the lithosphere then overprint the stress pattern associated with the cooling and early bending. Note that the lithospheres of the models with a free surface exhibit bending stresses that are order of magnitude larger than in the previously discussed simulations with a free slip upper boundary.

Fig. 8 shows vertical profiles of effective stress (horizontally averaged) in both models $M_{\rm vis}$ and $M_{\rm el}$, evenly sampled over the first 3 Gyr. It demonstrates thickening of the viscous lithosphere with a typical bending/unbending pattern (left panel) while the viscoelastic lithosphere with generally lower stresses shows preservation of the bending pattern of the initially thin lithosphere (right panel). Note that the stresses associated with bending of the 30 km thick lithosphere are in tens of MPa, while we observed stresses of only a few MPa in the free-slip surface simulations. In the viscoelastic model, the stresses below the 30 km depth are similar as in the free-slip case.

After examining the effects of lithospheric thickening, let us now look at the models in which the lithosphere is initially thick ($d_{\rm TB} = 300$ km). Such models display no differences between viscous and viscoelastic rheology, in case that a free slip condition is prescribed at the top (Section 4.2 above). In free surface models we do observe differences, but of a different nature than the stress memory effect described above.

In these models, the lithosphere is thinning and the layered stress structures thus could not develop here. The stress patterns are dominated by the bending stresses, and these are significantly smaller for the viscoelastic simulations (see the last paragraph of Section 3.2 and Fig. 3). We demonstrate this in Fig. 9, which shows the time evolution of the effective stress in E-models within a 3 Gyr long time window taken 12 Gyr after the initiation of the simulation.

Further evolution of the models is characterized by similar stress profiles as depicted in Fig. 9—the stress reduction is a general characteristic of statistically steady state viscoelastic convection with a free surface (i.e. regardless of the value of $d_{\rm TB}$), as long as the lithosphere is bending and unbending in the reached statistically steady state.

For the M-models the statistically steady states are almost stationary, with a stable plume in the centre and downwellings at the sides. Due to this steady loading the lithosphere is permanently bent, and not flexing up and down as in the previous case. It then reaches the

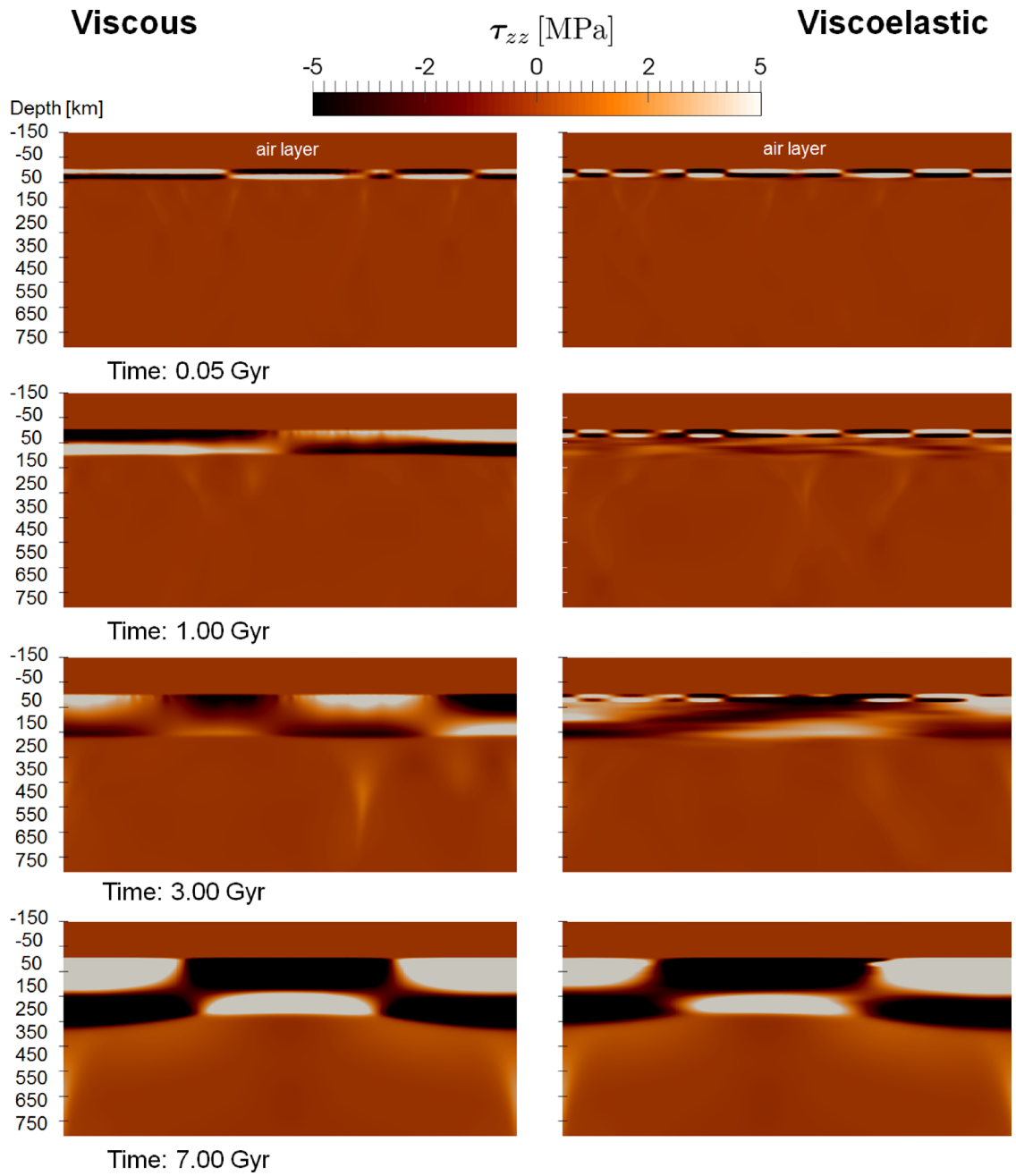

Figure 7. Vertical component of deviatoric stress τ_{zz} in model M with aspect ratio 1, $T_0 = 1900$ K, $d_{\mathrm{TB}} = 30$ km and a free surface. Stress scale is clipped for better visibility of the memory effect. Negative depths (in km) show the sticky air layer.

viscous limit and the effects of viscoelasticity disappear (*cf.* the last snapshot in Fig. 7).

Table 2 summarizes how the viscoelastic effects depend on the initial and boundary conditions. Both effects are stronger when the vigour of convection is higher.

4.4 Robustness of the results

The results presented above were obtained in a 2-D Cartesian geometry with aspect ratio 1. In order to estimate the effects of model geometry we repeated some of the simulations also in aspect ratio 4, 2-D spherical annulus (Hernlund & Tackley 2008), and 3-D Cartesian box. Based on these tests we can conclude that the stress memory and the stress reduction effects discussed in previous sections are robust, though the stress amplitudes differ in different geometries (*cf.* Fig. 10).

In agreement with studies by Thielmann *et al.* (2015) and Muhlhaus & Regenauer-Lieb (2005) the sublithospheric mantle convection was hardly affected by viscoelasticity or a free surface in our simulations. This does not imply that the internal dynamics were equivalent for each pair (viscous vs. viscoelastic) of the simulations we performed. Due to the chaotic nature of thermal convection we observed that some models get locked into a quasi-stable statistically steady state for up to billions of years (e.g. having more, or distorted, convection cells when compared to the stable statistically steady state). To our experience the likelihood of such behaviour was not affected by the inclusion of viscoelasticity and we avoided such cases in the presented work.

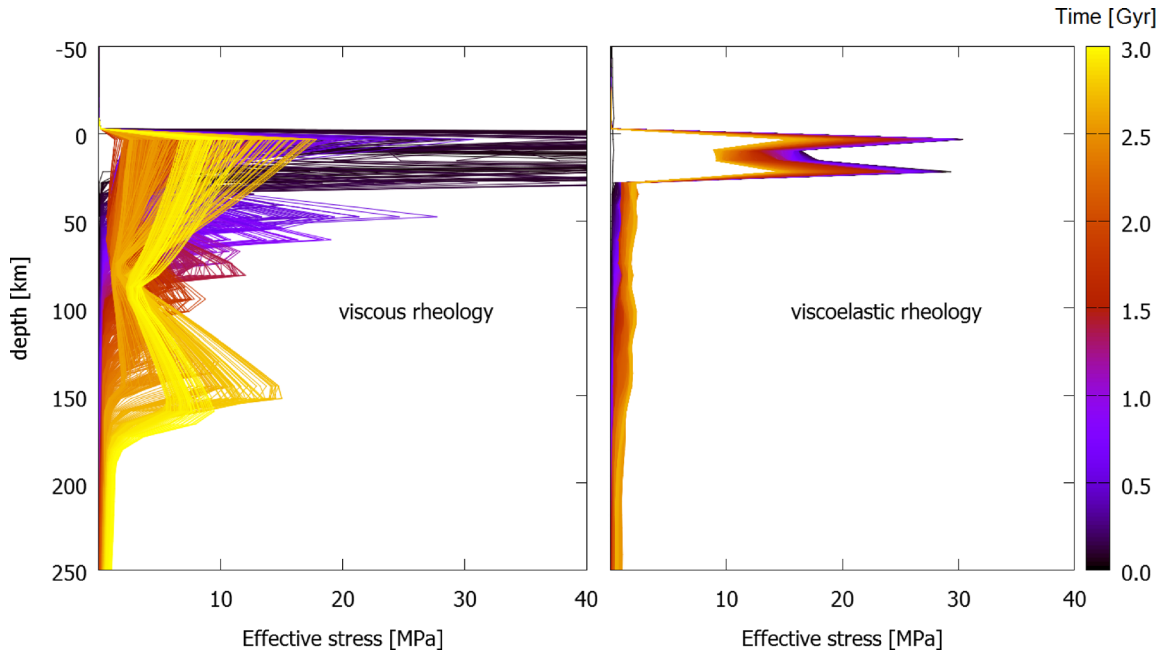

Figure 8. Temporal evolution of effective stress τ_{eff} in models M_{vis} and M_{el} with the same parameters as in Fig. 7. We show horizontally averaged radial profiles that are evenly sampled in time. Colour represents the time in Gyr, only the transient behaviour is shown.

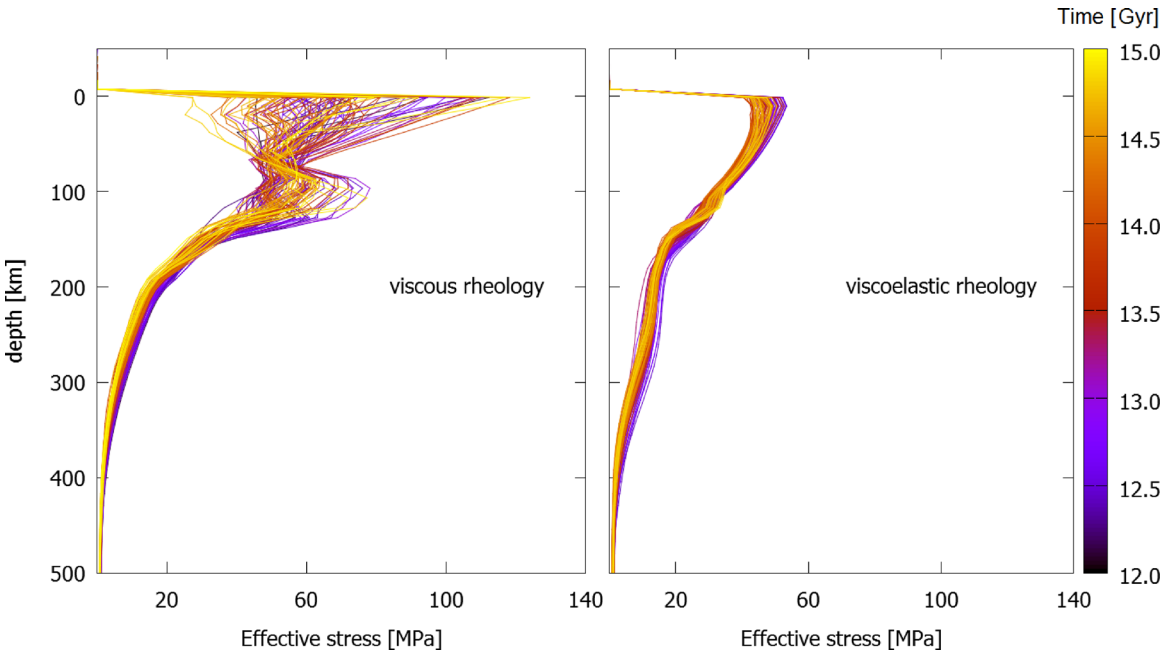

Figure 9. Temporal scatter of effective stress τ_{eff} in models E_{vis} and E_{el} with aspect ratio 1, $T_0 = 1900$ K, $d_{\text{TB}} = 300$ km and a free surface. We show 100 horizontally averaged depth profiles that are evenly sampled in time. Colour represents the time in Gyr.

5 DISCUSSION

We present here the results of numerical experiments focused on the effects of viscoelasticity on the stress and surface topography development of internally loaded lithosphere. First, we use the compositional model of a cylinder rising below the stiff lithosphere introduced by Crameri *et al.* (2012) and we extended their analysis for a viscoelastic stiff lid and also for higher lithospheric viscosities. We demonstrate that while for lower lithospheric viscosity (10^{23} Pa s) the IVF topography (from a free-slip model) is in good agreement with free surface topography, for higher lid viscosities the differences between free-slip and free-surface models significantly increase. These differences, that is, the error of the instantaneous IVF approach, are largely reduced if the lid is viscoelastic. Similar conclusions were made by Zhong (2002) for stationary loading.

Second, we performed thermal convection models focused on the evolution of planetary mantles. Lithospheric stresses were shown to differ considerably. If a free surface is prescribed and stiff lithosphere is thus able to bend and build topography, then viscoelastic models generally show lower stress amplitudes than purely viscous models. If a planetary mantle is cooling from an initially hot state with a thin lithosphere, then the memory effects associated with

Table 2. Summary of the viscoelastic effects in stagnant lid convection.

Model characteristics	'Frozen-in' stresses	Stress reduction
Free-slip, initially thick lithosphere	No	No
Free-slip, initially thin lithosphere	Yes	No
Free surface, initially thick lithosphere	No	Yes
Free surface, initially thin lithosphere	Yes	Yes

viscoelastic deformation result in a complex layered stress pattern, in which the shallower layers reflect preceding sublithospheric convective features active during the earlier stages of the model evolution. These frozen-in stresses remain visible on a time scale comparable to the Maxwell relaxation time of the lithosphere. The described phenomenon is thus a transient feature and depends on the initial temperature distribution. It is clearly favoured by the initially thin thermal boundary layer that may result from cooling of a magma ocean (Solomatov 2007). The vigour of the initial convection increases the observed complexity of the stress structure that is being recorded in the cooling and thickening lithosphere.

Thielmann *et al.* (2015) also observe non-smooth deviatoric stresses, while presenting simulations with surface Deborah numbers up to $De_s = 10^5$. Since the Deborah number is given by the ratio of the lithosphere's viscoelastic relaxation time to the diffusion time, it takes approximately De_s diffusion times for the stresses to relax from a certain state. The simulations presented in Thielmann *et al.* (2015) do not last multiples of the diffusion times, thus it is likely that the stress state of the lithosphere is largely influenced by the initial conditions, even though it cannot be seen from the Nusselt numbers or average velocity of the flow.

The key parameter controlling the importance of the memory effect is the Maxwell relaxation time of the lithosphere. The viscosity of the crust and lithosphere that determines the relaxation time is, however, largely unknown. Its estimates based on postglacial rebound inversions only give a lower bound, since the glacial cycle occurs on a time scale of about 100 kyr. Layers with t_M larger than 100 kyr behave effectively as an elastic material to such loading (see Section 3) and GIA (glacial isostatic adjustment) inversions are thus insensitive to higher viscosities. The fact that subduction or loading due to sedimentation are successfully modelled using a thin elastic plate theory again provides only the lower bound on the viscosity, in the sense that that t_M must be larger than the characteristic time of these phenomena.

In our simulations the Maxwell relaxation time of the lithosphere was determined by the upper viscosity cut-off. Lowering its value directly decreases the importance of the medium's memory. The ability to quickly deform in an elastic manner remains intact. One may thus expect the stress reduction effect to be independent on cut-off viscosity. However, less stiff purely viscous lids show smaller resistance when compared to more stiff purely viscous ones, and decreasing the cut-off value thus reduces the importance of both the stress memory and the stress reduction when comparing viscous and viscoelastic models with the same lithospheric viscosities. In a limited extent we still observed both effects when lowering η_{max} down to 10^{25} Pa s in thermal convection simulations with a free surface.

The models presented here were designed to investigate the basic effects of viscoelasticity on the evolution of a stiff planetary lid. As such they suffer from several simplifying assumptions. The first and probably major one is that the rheological description does not include any form of plastic yielding, even though the brittle failure and ductile yielding are important deformation mechanisms in the lithosphere and limit the resulting stresses. The second one is the simple Boussinesq approximation of the energy equation that does not account for shear heating. Viscous dissipation could play an important role in strain localization in a visco-elasto-plastic model (e.g. Schmalholz & Duretz 2015). In particular, it was recently shown by Jaquet *et al.* (2016) that the release of elastic energy promotes faulting induced by thermal softening. On the basis of our results we may speculate that yielding or thermal softening would occur on shorter wavelengths in the models that include viscoelasticity. Especially in the early stages of planetary evolution, when their thermal boundary layer is thin, viscoelasticity in combination with plasticity could dramatically affect lithospheric deformation or regime of convection. Indicative in this regard may be the results by Muhlhaus *et al.* (2006), who demonstrate an increase in the frequency of overturns in the episodic lid regime due to elasticity. Such a scenario should in future be tested in visco-elasto-plastic models in three-dimensional spherical geometry.

Despite the above mentioned simplifications we believe that our models demonstrate that including viscoelasticity is important if

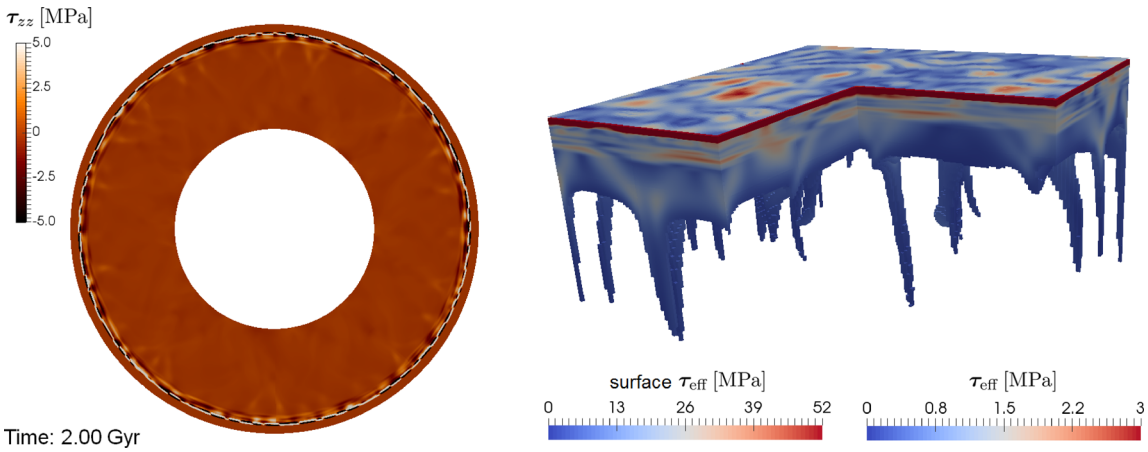

Figure 10. Model M_{el} with $T_0 = 1900$ K, $d_{TB} = 30$ km and a free surface after 2 Gyr, computed in 2-D spherical annulus (left) and 3-D Cartesian (right) geometries. Air is not shown in the 3-D model in order to reveal the surface stresses and the model domain is thresholded by an isotherm of 1670 K to show the spatial distribution of the downwellings. The stress scale is clipped in both cases to enhance the visibility of the subsurface layered structures, with the exception of the surface stresses in the 3-D simulation that are shown in their full range.

stress evolution and deformation of the lithosphere in models of planetary mantles are addressed.

ACKNOWLEDGEMENTS

VP acknowledges the support from the Sciex project No. 13.250 and the Charles University grant SVV260327/2016. We thank Louis Moresi, Thibault Duretz and an anonymous reviewer for helpful comments that significantly improved the manuscript, and Marcel Thielmann for insightful discussions and help with benchmarking the code.

REFERENCES

Beuchert, M.J. & Podladchikov, Y.Y., 2010. Viscoelastic mantle convection and lithospheric stresses, *Geophys. J. Int.,* **183**(1), 35–63.

Crameri, F. & Tackley, P.J., 2014. Spontaneous development of arcuate single-sided subduction in global 3-D mantle convection models with a free surface, *J. geophys. Res.,* **119**(7), 5921–5942.

Crameri, F. *et al.*, 2012. A comparison of numerical surface topography calculations in geodynamic modelling: an evaluation of the sticky air' method, *Geophys. J. Int.,* **189**(1), 38–54.

Duretz, T., May, D.A., Gerya, T.V. & Tackley, P.J., 2011. Discretization errors and free surface stabilization in the finite difference and marker-in-cell method for applied geodynamics: a numerical study, *Geochem. Geophys. Geosyst.,* **12,** doi:10.1029/2011GC003567.

Gerya, T., 2010. *Introduction to Numerical Geodynamic Modelling,* Cambridge Univ. Press.

Gerya, T.V. & Yuen, D.A., 2007. Robust characteristics method for modelling multiphase visco-elasto-plastic thermo-mechanical problems, *Phys. Earth planet. Inter.,* **163**(1–4), 83–105.

Golle, O., Dumoulin, C., Choblet, G. & Cadek, O., 2012. Topography and geoid induced by a convecting mantle beneath an elastic lithosphere, *Geophys. J. Int.,* **189**(1), 55–72.

Harder, H., 1991. Numerical-simulation of thermal-convection with Maxwellian viscoelasticity, *J. Non-Newton. Fluid Mech.,* **39**(1), 67–88.

Hernlund, J.W. & Tackley, P.J., 2008. Modeling mantle convection in the spherical annulus, *Phys. Earth planet. Inter.,* **171**(1–4), 48–54.

Ivins, E., Unti, T. & Phillips, R., 1982. Large Prandtl number finite-amplitude thermal-convection with Maxwell viscoelasticity, *Geophys. Astrophys. Fluid Dyn.,* **22**(1–2), 103–132.

Jaquet, Y., Duretz, T. & Schmalholz, S.M., 2016. Dramatic effect of elasticity on thermal softening and strain localization during lithospheric shortening, *Geophys. J. Int.,* **204**(2), 780–784.

Kaus, B.J.P., Muehlhaus, H. & May, D.A., 2010. A stabilization algorithm for geodynamic numerical simulations with a free surface, *Phys. Earth planet. Inter.,* **181**(1–2), 12–20.

Kiefer, W., Bills, B. & Nerem, R., 1996. An inversion of gravity and topography for mantle and crustal structure on Mars, *J. geophys. Res.,* **101**(E4), 9239–9252.

Liu, I.-S. & Sampaio, R., 2014. Remarks on material frame-indifference controversy, *Acta Mechanica,* **225**(2), 331–348.

Matsumoto, T. & Tomoda, Y., 1983. Numerical-simulation of the initiation of subduction at the fracture-zone, *J. Phys. Earth,* **31**(3), 183–194.

Moresi, L., Dufour, F. & Muhlhaus, H., 2002. Mantle convection modeling with viscoelastic/brittle lithosphere: numerical methodology and plate tectonic modeling, *Pure appl. Geophys.,* **159**(10), 2335–2356.

Moresi, L., Dufour, F. & Muhlhaus, H., 2003. A Lagrangian integration point finite element method for large deformation modeling of viscoelastic geomaterials, *J. Comput. Phys.,* **184**(2), 476–497.

Muhlhaus, H. & Regenauer-Lieb, K., 2005. Towards a self-consistent plate mantle model that includes elasticity: simple benchmarks and application to basic modes of convection, *Geophys. J. Int.,* **163**(2), 788–800.

Muhlhaus, H.-B., Davies, M. & Moresi, L., 2006. Elasticity, yielding and episodicity in simple models of mantle convection, *Pure appl. Geophys.,* **163**(9), 2031–2047.

Schmalholz, S.M. & Duretz, T., 2015. Shear zone and nappe formation by thermal softening, related stress and temperature evolution, and application to the Alps, *J. Metamorphic Geol.,* **33**(8, SI), 887–908.

Schmeling, H. *et al.*, 2008. A benchmark comparison of spontaneous subduction models - towards a free surface, *Phys. Earth planet. Inter.,* **171**(1–4, SI), 198–223.

Solomatov, V., 1995. Scaling of temperature-dependent and stress-dependent viscosity convection, *Phys. Fluids,* **7**(2), 266–274.

Solomatov, V., 2007. 9.04 - magma oceans and primordial mantle differentiation, in *Treatise on Geophysics,* pp. 91–119, ed. Schubert, G., Elsevier.

Tackley, P.J., 2008. Modelling compressible mantle convection with large viscosity contrasts in a three-dimensional spherical shell using the Yin-Yang grid, *Phys. Earth planet. Inter.,* **171**(1–4, SI), 7–18.

Thielmann, M., Kaus, B.J.P. & Popov, A.A., 2015. Lithospheric stresses in Rayleigh-Benard convection: effects of a free surface and a viscoelastic Maxwell rheology, *Geophys. J. Int.,* **203**(3), 2200–2219.

Turcotte, D. & Schubert, G., 2002. *Geodynamics,* Cambridge Univ. Press.

Vaz, M., Jr., Munoz-Rojas, P.A. & Filippini, G., 2009. On the accuracy of nodal stress computation in plane elasticity using finite volumes and finite elements, *Comput. Struct.,* **87**(17–18), 1044–1057.

Zhong, S., 2002. Effects of lithosphere on the long-wavelength gravity anomalies and their implications for the formation of the Tharsis rise on Mars, *J. geophys. Res.,* **107**(E7), doi:10.1029/2001JE001589.

APPENDIX A: BENCHMARK TESTS

Our implementation of viscoelasticity was verified using two benchmark tests: (i) a stationary viscoelastic flow in a 2-D box with aspect ratio 1 (Harder 1991) and (ii) the deformation of an elastic slab embedded in a viscous medium (Gerya 2010).

A1 Thermal convection of an isoviscous Maxwell fluid

In this benchmark we test the implementation of the advection and corotation of the stress. We perform the simulation of thermal convection of an isoviscous Maxwell fluid in a 1×1 Cartesian box. We assume the Boussinesq approximation and reproduce results of Harder (1991) for Rayleigh number 9487 and Deborah number 1.5×10^{-3} (Fig. A1) on a mesh with 40×40 grid points. We make a visual comparison of the isolines of vorticity, temperature, deviatoric shear stress and normal stress difference (the exact values of isolines are stated in Harder 1991).

In reproducing the stationary flow it is important to realize that the Weissenberg number, $W_{ei} := 2De\|\mathbb{D}\|D^2/\kappa$, is close to 1 for $De = 1.5 \times 10^{-3}$ and the given model setup. A Maxwell body with Jaumann's rate chosen as the stress rate (i.e. the medium we study) exhibits shear softening in a simple shear flow for Weissenberg number greater than 1 (see Muhlhaus & Regenauer-Lieb (2005) for details) and shear softening leads to numerically unstable solutions. The viscoelastic convection simulation thus needs to be started from a state which is close to the stationary solution (e.g. from the viscous stationary solution), in order not to exceed the critical Weissenberg number when reaching the final state.

For Deborah numbers higher than 1.5×10^{-3} we no longer reach a stationary solution and the simulations become numerically unstable (the velocities go to infinity). Setting a lower bound on the time step used in the rheological eqs (11)–(13) prevents such instabilities, largely extending the range of Deborah numbers that can be modelled. Detailed analysis of the problem is beyond the scope of this paper—in the convection simulations of planetary bodies presented in the main text we are far from the critical Weissenberg number.

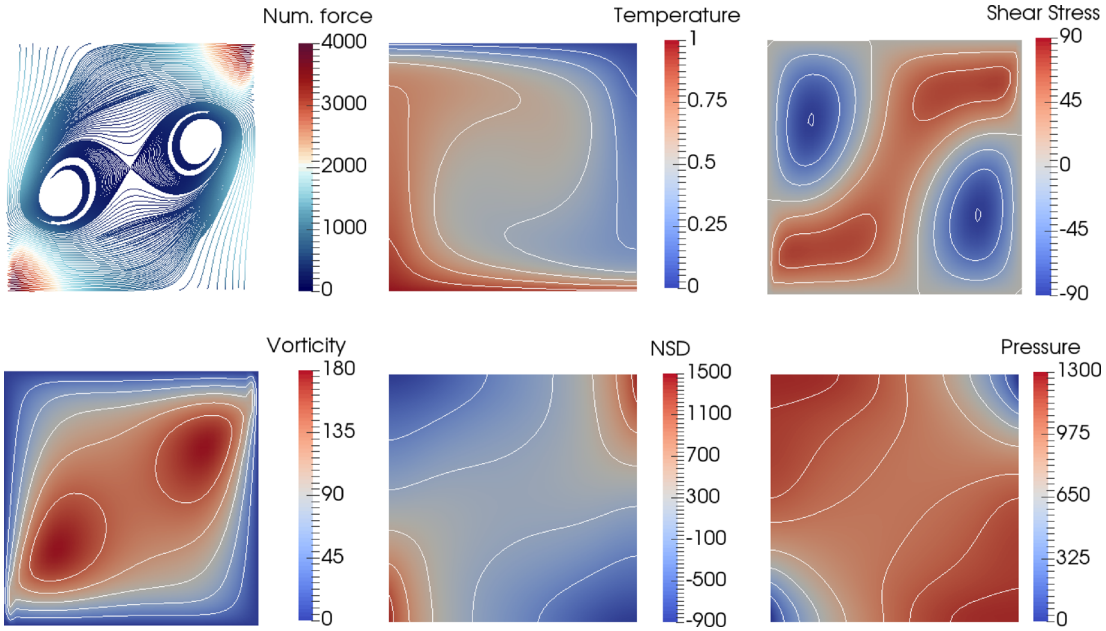

Figure A1. Stationary flow of an isoviscous fluid in a 40 × 40 box with free slip boundaries, $De = 0.0015$. See Harder (1991) for comparison with a viscous solution and for exact values of the isolines. Left top picture shows streamlines of the extra force term $\nabla \cdot [(1 - Z)\check{\boldsymbol{\tau}}^{n-1}]$, middle picture in the bottom row displays normal stress differences.

In this benchmark test we used a grid-based donor cell advection technique instead of the tracer based advection scheme applied in all other calculations. Tracer based advection of stress does not perform well in this case, due to the high vorticity gradient in the corners of the box (in combination with the low resolution of the mesh). The number of tracers per cell needed to produce results comparable to the grid-based approach is over 1000 here. The time step was governed by the CFL stability criterion.

A2 Recovery of the original shape of an elastic slab

Following Gerya (2010) we further examine the deformation of a hanging slab due to gravitational force. An effectively elastic slab, attached to the left boundary, is being steadily deformed over 20 kyr by gravity ($g = 10\ \mathrm{m\ s^{-2}}$). After 20 kyr gravity is switched off and the original shape of the slab is recovered. The slab viscosity is 10^{27} Pa s and its shear modulus is 10^{10} Pa. The effectively viscous medium that surrounds the slab has a viscosity of 10^{21} Pa s and a shear modulus of 10^{20} Pa. The density of the slab is 4000 kg $\mathrm{m^{-3}}$ while the surrounding material has a density of 1 kg $\mathrm{m^{-3}}$. Extreme discontinuities in material parameters are treated using harmonic averaging of the shear modulus in order to avoid high numerical viscosity on the interfaces (Gerya 2010). A resolution of 128 × 128 nodes with 100 particles per cell was used, time step of 2 yr was being gradually increased after reaching 30 kyr. Results are summarized in Fig. A2(a). The elastic (relaxation time ∼3 Gyr) slab fully recovered its shape while the viscous medium sustained permanent deformation.

This particular example is rather challenging as the model includes sharp interfaces with strongly varying properties. Numerical diffusion has to be kept to a minimum when treating advection of quantities, including the stresses, in order to retain clear interfaces as the slab is being deformed and then relaxed to its original position. While both methods that we tested, that is, donor cell scheme and storing stress on tracers, lead to a perfect recovery of the slab for the case described above, the methods begin to differ if gravity is applied longer than for 20 kyr. Fig. A2(b) compares the recovery obtained when the gravity was switched off only after 35 kyr (still a negligible time with respect to the relaxation time of the slab). We see that numerical diffusion has slightly distorted the recovery when grid-based donor cell method was used, especially near the unattached corners of the slab. Quantities other than the stress (η, μ and ρ) were carried on tracers in both cases.

Parts of the slab experience significant rigid body rotation during the studied process and the corotational term in eq. (7) is thus crucial—omitting it would lead to distorted recovery of the slab.

APPENDIX B: SUBGRID OSCILLATIONS OF STRESS

Similarly to advection of the temperature field, the problem with treating advection of stresses using the incremental update scheme by Gerya & Yuen (2007) is that stress jumps on adjacent markers, resulting from flow-induced stirring, cannot be damped out by grid-scale corrections.

Fig. B1 shows an example of such oscillations in a thermal convection simulation. The viscoelasticity parameter Z is close to one (cca. 0.8) in the circled region and the stress should thus be governed by the viscous creep, forming relatively smooth patterns. However, tracers with a different stress history are transported close to each other in the selected region. The grid-scale updates of stresses (eqs 22 and 23 in Gerya & Yuen 2007) cannot relax such subgrid stress differences and result in the depicted unphysical oscillations of the stress field. The likelihood of such oscillatory behaviour increases with increasing resolution and with the number of tracers per cell.

In our modification of the algorithm designed by Gerya & Yuen (2007), we use directly eq. (11) to evaluate the stress tensor on each tracer. First, the tracers are advected and the corotational term, computed on the grid, is interpolated to them. Then, the value of the viscoelasticity parameter is computed on the grid and interpolated to each tracer, so that we can multiply the stress on each tracer

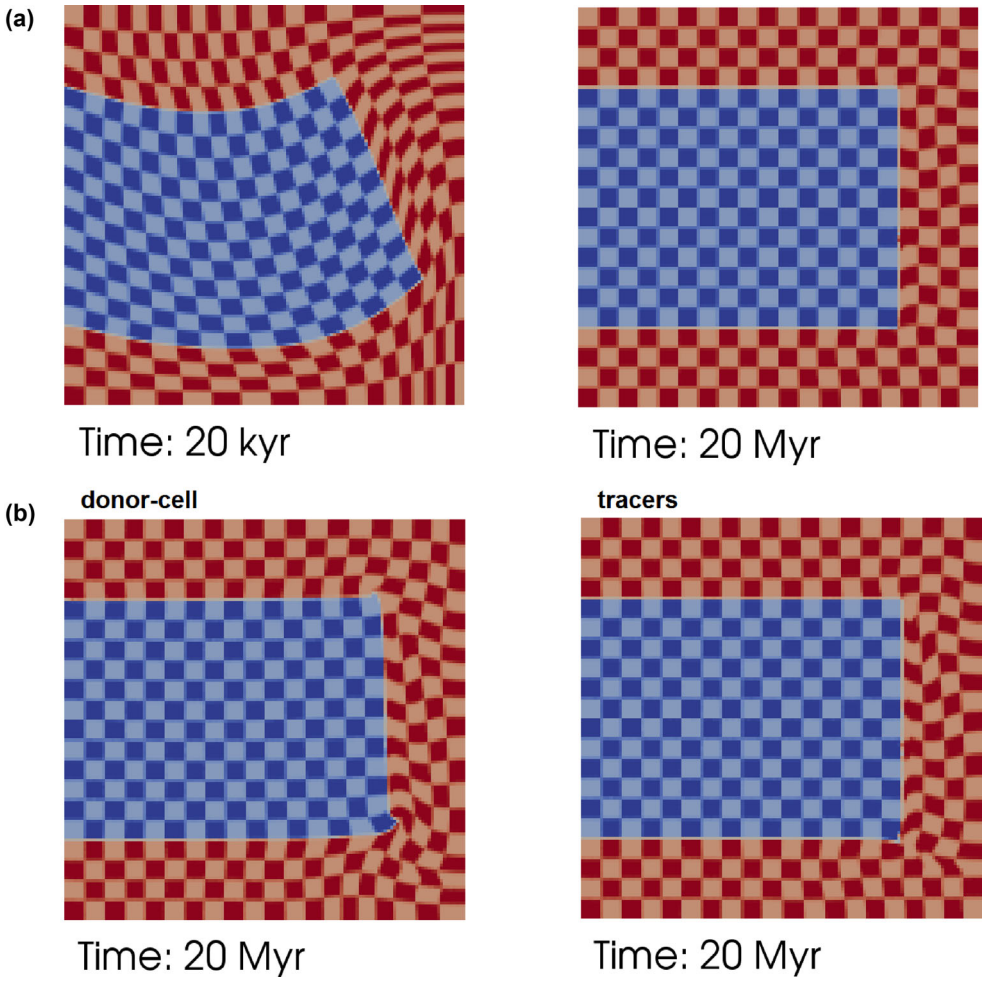

Figure A2. (a) Reproduction of numerical experiment by Gerya (2010). A slab with high viscosity of 10^{27} Pa s and shear modulus 10^{10} Pa is attached to the left boundary and surrounded by a weak viscoelastic medium with viscosity 10^{21} Pa s and shear modulus 10^{20} Pa. Density of the slab is 4000 kg m^{-3}, density of the surroundings is only 1 kg m^{-3}. (b) Comparison of the numerical methods used for advection of stresses. Gravity is switched off after 35 kyr and not 20 kyr as in the upper case, left panel shows the recovery when grid-based donor cell method is applied, right panel shows the recovery when tracers are used to advect the stresses.

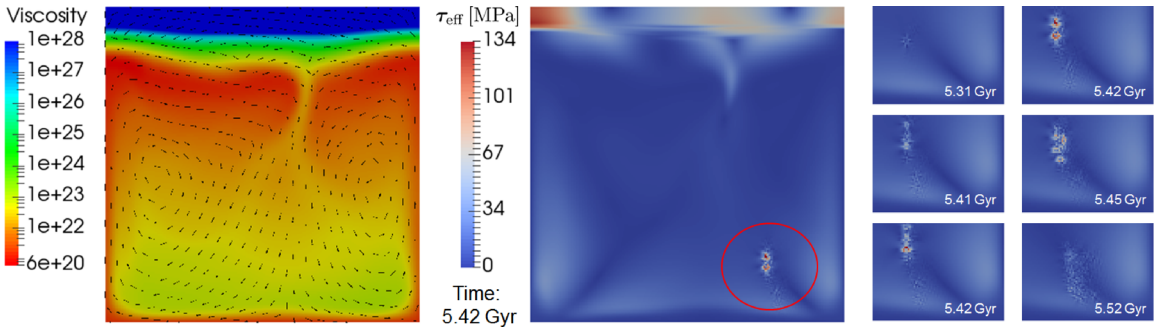

Figure B1. Stress oscillations in a viscoelastic thermal convection. Red circle points to the oscillatory behaviour, right panel zooms in the respective part of the model domain in a sequence of time steps. Model parameters are the same as in Fig. 4 from the main text.

by $(1 - Z)$. Finally, the term $2Z\eta\mathbb{D}^n$ is computed on the grid and interpolated to each tracer.

In regions with Z close to 1, the procedure leads to practically re-setting the value of stress on each tracer to $2Z\eta\mathbb{D}^n$ at each time step, and two adjacent tracers will thus carry similar stress tensors after the procedure, even if before there was a mutual stress jump (consequently, the oscillations as depicted in Fig. B1 are not observed). In regions with Z close to 0, the procedure behaves as an incremental update scheme: the stress tensor changes only slightly on each tracer and mutual stress differences among the tracers are preserved. This is important as interpolating the entire stress (instead of the stress change) from grid to tracers would lead to spurious numerical diffusion in such regions.